AIMS Mathematics

https://www.aimspress.com/journal/Math

AIMS Mathematics, 11(3): 7183–7206.
DOI: 10.3934/math.2026296
Received: 06 February 2026
Revised: 12 March 2026
Accepted: 16 March 2026
Published: 19 March 2026

Research article

Stability analysis and L1-finite difference modeling of inverse problems for fractional Schrödinger equations with variable diffusion

Mousa J. Huntul[1,*], **Mahmut Modanli**[2,*], **and Mohammad Izadi**[3]

[1] Department of Mathematics, College of Science, Jazan University, P.O. Box 114, Jazan 45142, Saudi Arabia
[2] Department of Mathematics, Faculty of Arts and Sciences, Harran University, Şanlıurfa 63300, Türkiye
[3] Department of Applied Mathematics, Faculty of Mathematics and Computer Science, Shahid Bahonar University of Kerman, Kerman, Iran

* **Correspondence:** Email: mhantool@jazanu.edu.sa; mmodanli@harran.edu.tr.

Abstract: This study developed a finite difference method (FDM) for a time-fractional inverse problem associated with Schrödinger partial differential equations. The main objective of the inverse problem is the simultaneous identification of the unknown source function $p(x)$ and the state variable $w(t, x)$. The mathematical model involves the Caputo fractional order derivative (CFOD) of order $0 < \alpha \leq 1$ and incorporates a spatially variable diffusion coefficient $a(x)$, which significantly increases the complexity of the problem compared with constant-coefficient models. Homogeneous Dirichlet boundary value conditions (DBVCs) were imposed on the spatial domain. For the numerical discretization, the time-CFOD was approximated using a consistent L1-type scheme, while the spatial derivatives were discretized by second-order central finite difference schemes (FDSs). Stability estimates and convergence properties of the proposed numerical scheme are rigorously established using discrete energy techniques. The analysis shows that the method achieves a convergence order of $O(\tau^{2-\alpha} + h^2)$. To validate the theoretical results, numerical experiments were performed for two benchmark problems with diffusion coefficients $a(x) = x^2+1$ and $a(x) = x^3+1$. The obtained numerical results confirm the effectiveness and robustness of the proposed approach. Graphical comparisons illustrate the behavior of solutions for different fractional orders as time evolves, while error tables demonstrate that the fractional-order solutions provide more accurate approximations to the exact solution than the corresponding integer-order case.

Keywords: fractional diffusion equation; Caputo derivative; inverse Schrödinger problem; finite difference method; stability; convergence
Mathematics Subject Classification: 35R30, 35A01, 65N12

1. Introduction

Over the past decades, fractional partial differential equations (FPDEs) have garnered significant interest owing to their ability to model hereditary and memory properties found in numerous biological, physical, mechanical, and engineering processes. Applications naturally arise in fields such as anomalous diffusion, viscoelastic materials, groundwater flow, signal processing, and financial mathematics. The growing theoretical and computational interest in FPDEs has led to the development of various analytical and numerical methods for their solution. Recent works include stability analyses and numerical schemes for fractional telegraph equations [1], the inverse problems for identifying time-dependent terms in fractional diffusion models [2, 3], and robust semi-analytical techniques for nonlinear fractional equations such as the Burgers-Huxley and Schrödinger equations [4, 5]. Spectral and wavelet-based approaches have also been widely employed; for instance, Gegenbauer wavelets for nonlinear Klein-Gordon equations [6], generalized Jacobi-Galerkin methods for multi-term diffusion-wave equations [7], and Haar wavelet techniques for fractional advection-diffusion equations [8].

In the context of fractional Schrödinger-type equations, which are of particular interest in quantum mechanics and wave propagation with memory effects, both decomposition methods and FDSs have been investigated. For example, Modanli and Bajjah [9] studied a time-fractional Schrödinger equation using a double Laplace decomposition method combined with the FDM. Despite these advances, the numerical solution of inverse time-fractional Schrödinger-type equations, especially those with variable diffusion coefficients, remains a challenging and relatively underexplored area. Such inverse problems are inherently ill-posed and require carefully designed stable numerical schemes. Fractional-order Schrödinger partial differential equations (FOSPDEs) are attracting increasing interest due to their ability to model memory and inheritance effects arising in quantum diffusion, anomalous transport, and non-local interactions [10]. When such models are combined with inverse problems where unknown parameters or source terms need to be defined from limited observations, analytic solutions become impractical or unusable. This motivates the development of robust and accurate numerical techniques. Among various approaches, the FDM offers a systematic and efficient framework for decomposing fractional operators while preserving the fundamental physical structure of the governing equation. Its flexibility in handling inverse formulations, its stability under grid refinement, and its compatibility with fractional time derivatives make it particularly suitable for solving fractional inverse Schrödinger-type problems.

Among FOSPDEs, time-dependent fractional diffusion and the inverse problems play a significant role in describing diffusion processes with non-local temporal behavior. Compared to classical integer-order equation models, fractional-order models provide a more accurate description of long-range temporal dependence. The non-local structure of fractional derivatives fundamentally hinders both analytical progress and the development of efficient numerical methods. In this study, we focus on a class of inverse initial boundary value problems (IBVPs) governed by FOSPDEs. Our aim is to construct a stable and convergent finite difference scheme (FDS) that can accurately capture the solution behavior for different spatially varying diffusion coefficients. Based on both their theoretical importance and practical relevance, we examine two representative cases: $a(x) = x^2 + 1$ and $a(x) = x^3 + 1$.

The following points summarize the core contributions of the current study:

- An FDM discretization for time-fractional and space diffusion inverse Schrödinger problems is constructed.
- Rigorous stability estimates and convergence results have been achieved.
- Obtained numerical simulations with MATLAB to validate the theoretical analysis for multiple diffusion profiles.

Many studies have been conducted in the literature regarding the inverse problems for PDEs. In [11], the authors investigated a time-dependent source identification problem based on integral overdetermination. They established stability and coercive stability inequalities for the solution and employed an FDM to compute approximate solutions for the inverse elliptic problem subject to DBVCs [12]. Using positive-definite operators in a self-adjoint Hilbert space, the stability of the time-dependent source identification problem for the Schrödinger equation was established in [13]. Subsequently, [14] addressed the inverse problem of recovering a stationary source for the Schrödinger evolution in a bounded domain of $\mathbb{R}^N$ under DBVCs, using a single time-dependent Neumann boundary measurement to account for a discontinuous principal coefficient $a(x)$. Further contributions include the study of initial and NBVC problems for linear one-dimensional time FOSPDEs of order $\alpha \in (0, 1]$ in the Caputo sense [15]. Similarly, one-dimensional linear time-dependent Schrödinger and IBV problems were investigated in [16]. Recent applications of the inverse problems extend to precision alignment in optics, where inverse methods were used to determine the relative orientation of space mirrors [17], and to the extraction of implicit field costs via inverse optimal transport models [18]. The inverse problem of identifying space- and time-dependent source terms in the Schrödinger equation with dynamic boundary conditions from final data was studied in [19]. In a related context, [20] investigated the recovery of a time-dependent source term for the heat equation governed by two NBVCs. More broadly, the inverse problems for fractional differential equations have attracted considerable attention. For instance, Huntul [21] studied inverse source problems for multi-parameter space-time fractional equations involving bi-fractional Laplacian operators. Higher-order models have also been considered; for example, the inverse recovery problem for sixth-order Boussinesq-Love equations was addressed using septic B-splines in [22]. From a computational perspective, hybrid projection strategies for large-scale inverse model problems were surveyed by Chung and Gazzola [23], highlighting modern numerical techniques for such ill-posed problems. Robin boundary value problems and Bratu-type equations were studied by using a compact combination of second-kind Chebyshev polynomials [24]. They investigated a collocation-based numerical method for solving the third-order Gilson–Pickering equation (GPE) and the classical Rosenau-Hyman equation (RHE) [25]. The authors of [26] used specific polynomials to solve some DEs, which are generalizations of the first kind of Chebyshev polynomials.

Despite the substantial developments in the numerical analysis of PDEs, much of the existing research has mainly focused on direct problems with constant coefficients. However, inverse formulations for time-fractional Schrödinger-type equations have attracted comparatively less attention, particularly in the presence of spatially variable diffusion coefficients. The introduction of a variable diffusion coefficient leads to a non-uniform differential operator, which increases the complexity of both the mathematical analysis and the numerical implementation. In addition, the simultaneous identification of the unknown source function $p(x)$ and the state variable poses further computational challenges. Motivated by these issues, this study considers an inverse problem for time FOSPDEs with a variable diffusion coefficient $a(x)$ and an unknown spatial source $p(x)$. To efficiently approximate the solution, an FDS based on the L1-type discretization of the Caputo fractional order derivative (CFOD) is developed, and the stability and convergence properties of the proposed numerical method are rigorously analyzed. It is worth emphasizing that the present study considers a spatially variable diffusion coefficient $a(x)$, which distinguishes the proposed model from many existing studies that assume constant diffusion parameters. In practical physical systems, diffusion properties often vary across the spatial domain due to heterogeneity in the underlying medium. Incorporating a variable coefficient, therefore, provides a more realistic mathematical description of the process, but it also introduces additional analytical and numerical challenges since the governing operator becomes spatially non-uniform. The proposed numerical framework is designed to effectively handle this variability while maintaining stability and convergence of the solution.

In this study, the CFOD is adopted instead of the Riemann–Liouville derivative due to its suitability for modeling physical problems with classical initial conditions. In particular, the Caputo formulation allows the initial conditions to be expressed in terms of integer-order derivatives of the unknown function, which have clear physical interpretations in many applications. In contrast, the Riemann–Liouville derivative requires fractional-order initial conditions that are often difficult to interpret and implement in practical problems. For this reason, the Caputo derivative is widely preferred in the modeling of time-fractional evolution equations, including fractional Schrödinger-type models, where the initial state of the system is naturally given in terms of standard physical quantities.

In the current study, we examine an inverse problem governed by a time-FOSPDE. The mathematical model is described by

$$\mathrm{i}\,{}_0^C D_t^\alpha w(t,x) - \frac{\partial}{\partial x}\left(a(x)\frac{\partial w(t,x)}{\partial x}\right) = p(x) + f(t,x), \qquad (t,x) \in (0,T)\times(0,\ell), \tag{1.1}$$

where $\mathrm{i} = \sqrt{-1}$, ${}_0^C D_t^\alpha w(t,x)$ signifies the CFOD, $\alpha \in (0,1]$, $a(x) > 0$ is a spatially dependent diffusion coefficient, $p(x)$ is an unknown time-independent source, and $f(t,x)$ represents a known time-dependent source term. The unknowns of the inverse problem are the pair $(w(t,x), p(x))$ satisfying (1.1). Since the function $w(t,x)$ possesses the partial derivative $\frac{\partial w}{\partial t}$, it is continuous with respect to t on $[0,T]$. Therefore, the evaluation of $w(t,x)$ at a fixed time t is well-defined. The equation is supplemented with the initial and interior measurement conditions

$$w(0,x) = \phi(x), \qquad x \in [0,\ell], \tag{1.2}$$

$$w(\lambda,x) = \Phi(x), \qquad \lambda \in (0,T), \tag{1.3}$$

and homogeneous DVBCs

$$w(t,0) = 0, \qquad w(t,\ell) = 0, \qquad t \in [0,T]. \tag{1.4}$$

Here ${}_0^C D_t^\alpha w(t,x)$ stands for the fractional derivative in the notion of Caputo with order α. The CFOD α for a sufficiently smooth function $w(t,x)$ is defined as

$${}_0^C D_t^\alpha w(t,x) = \frac{1}{\Gamma(1-\alpha)}\int_0^t \frac{\partial w(\tau,x)}{\partial \tau}(t-\tau)^{-\alpha}\,d\tau, \qquad 0 < \alpha < 1. \tag{1.5}$$

In the limiting case $\alpha = 1$, the Caputo derivative reduces to the classical first-order derivative, namely,

$$ {}_{0}^{C}D_t^1 w(t,x) = \frac{\partial w(t,x)}{\partial t}. \tag{1.6}$$

The primary goal of the ongoing research study is to develop a stable and convergent FDS to solve the above inverse problem governed by an FOSPDE, and to analyze its numerical performance for different choices of the diffusion coefficient $a(x)$.

The remainder of this paper is organized as follows. In Section 1, the introduction and motivation for the study are presented. Section 2 provides the exact solution of the problem and establishes stability estimates for problem (1.1). In Section 3, an FDS is developed for the inverse problem associated with problem (1.1). Section 4 presents numerical results, including benchmark tests and error analysis, to validate the theoretical findings and figures. Finally, Section 5 concludes the paper with a summary of the main results and possible directions for future research.

2. Exact solution and stability estimates for the inverse problem

In this section, we present the exact solution of model problem (1.1) and establish stability estimates for both the solution $w(t,x)$ and the inverse source function $p(x)$.

2.1. *Abstract form for the exact solution*

Let the spatial operator be defined as follows:

$$\mathcal{A}w(x) := -\frac{\partial}{\partial x}\left(a(x)\frac{\partial w(x)}{\partial x}\right), \quad x \in (0,\ell),$$

where the domain $D(\mathcal{A})$ is given by

$$D(\mathcal{A}) = H^2(0,\ell) \cap H_0^1(0,\ell),$$

subject to the homogeneous DBVC

$$w(0) = w(\ell) = 0.$$

This ensures that $\mathcal{A}$ is self-adjoint and positive definite. Suppose that $a(x) \in C^1([0,\ell])$ and $a(x) \geq a_0 > 0$. Then the operator $\mathcal{A}$ admits eingenpairs $\{(s_n,\ r_n)\}_{n=1}^{\infty}$ satisfying $\mathcal{A}\, r_n(x) = \ s_n\, r_n(x), \quad r_n(0) = r_n(\ell) = 0$, where $\{\ r_n\}$ forms an orthonormal basis of $L^2(0,\ell)$ and $\ s_n > 0$. We expand the solution and the given data as follows:

$$w(t,x) = \sum_{n=1}^{\infty} W_n(t)\, r_n(x), \quad p(x) = \sum_{n=1}^{\infty} p_n\, r_n(x), \quad f(t,x) = \sum_{n=1}^{\infty} f_n(t)\, r_n(x). \tag{2.1}$$

By inserting the equations (2.1) into (1.1) yields the fractional ODE

$$\mathrm{i}\, {}_{0}^{C}D_t^{\alpha} W_n(t) + \ s_n W_n(t) = p_n + f_n(t), \quad 0 < \alpha \leq 1. \tag{2.2}$$

Using the Laplace transform method and formulas (2.1), one can find the exact solution of the model problem (2.2) as follows:

$$W_n(t) = \phi_n E_{\alpha}(\mathrm{i}\ s_n t^{\alpha}) - \mathrm{i}\int_0^t (t-\tau)^{\alpha-1} E_{\alpha,\alpha}(\mathrm{i}\ s_n (t-\tau)^{\alpha})\,(p_n + f_n(\tau))\,d\tau,$$

where $\phi_n = \langle \phi,\ r_n \rangle$ and E_α, $E_{\alpha,\alpha}$ are Mittag–Leffler functions. Finally, the exact solution of the model equation (1.1) is given by

$$w(t,x) = \sum_{n=1}^{\infty} \left[\phi_n E_\alpha(\mathrm{i}\ s_n t^\alpha) - \mathrm{i} \int_0^t (t-\tau)^{\alpha-1} E_{\alpha,\alpha}(\mathrm{i}\ s_n (t-\tau)^\alpha)\, (p_n + f_n(\tau))\, d\tau \right] r_n(x). \tag{2.3}$$

To avoid degeneracy of the diffusion operator and ensure the ellipticity condition $a(x) \geq a_0 > 0$, we choose the diffusion coefficient as $a(x) = x^2 + 1$ and $a(x) = x^3 + 1$. This guarantees $a(x) \geq 1$ for all $x \in [0, \pi]$, so that the stability estimates in the following Theorems 2.1 and 2.2 remain valid.

2.2. Stability estimate for the exact solution

Theorem 2.1 (Stability estimate with explicit dependence on α and T)**.** *Let $w(t,x)$ be the solution given by formula* (2.3)*. Suppose that $\phi \in L^2(0,\ell)$, $\quad p \in L^2(0,\ell)$, $\quad f \in L^2(0,T; L^2(0,\ell))$. Then, there exists a constant $C_\alpha(T) > 0$, depending explicitly on the fractional order α and the final time T, such that*

$$\|w(t,\cdot)\|_{L^2(0,\ell)} \leq C_\alpha(T)\Big(\|\phi\|_{L^2(0,\ell)} + \|p\|_{L^2(0,\ell)} + \|f\|_{L^2(0,t;L^2(0,\ell))} \Big), \quad t \in [0,T]. \tag{2.4}$$

Moreover, for any finite $T > 0$, the constant $C_\alpha(T)$ remains bounded and exhibits mild growth as $\alpha \to 0^+$.

Proof. Using the representation formula (2.3), the solution $w(t,x)$ can be expanded in terms of the eigenfunctions of the Laplace operator. The expansion coefficients involve Mittag–Leffler functions:

$$E_\alpha(i s_n t^\alpha), \qquad t^{\alpha-1} E_{\alpha,\alpha}(i s_n t^\alpha),$$

where λ_k are the eigenvalues and $i = \sqrt{-1}$. From known bounds for Mittag–Leffler functions with complex arguments (see, e.g., [27]):

$$|E_\alpha(i s t^\alpha)| \leq C_\alpha(T), \qquad |t^{\alpha-1} E_{\alpha,\alpha}(i s t^\alpha)| \leq C_\alpha(T), \quad t \in [0,T],$$

where the constant $C_\alpha(T)$ depends on α and the final time T. For finite T, $C_\alpha(T)$ remains bounded, and as $\alpha \to 0^+$, it shows mild growth due to the factor $t^{\alpha-1}$. Applying Parseval's identity and the triangle inequality to the series expansion gives

$$\|w(t,\cdot)\|_{L^2(0,\ell)} \leq C_\alpha(T)\Big(\|\phi\|_{L^2(0,\ell)} + \|p\|_{L^2(0,\ell)} + \|f\|_{L^2(0,t;L^2(0,\ell))} \Big),$$

which proves the stability estimate (2.4). □

Here, $C_\alpha > 0$ denotes a generic constant depending only on the fractional order α (and possibly on T and the coefficient $a(x)$), but independent of w, ϕ, p, and f.

2.3. Stability inequality for the inverse source

Suppose that the final-time observation

$$w(\lambda, x) = \Phi(x), \quad \lambda \in (0,T],$$

is given.

Theorem 2.2 (Conditional stability of the inverse source)**.** *Assume* $w(\lambda, x) = \Phi(x)$ *is present and suppose the hypotheses of the previous theorem hold. Then the inverse source* $p(x)$ *satisfies the following stability inequality:*

$$\|p\|_{L^2(0,\ell)} \leq C\left(\|\Phi\|_{L^2(0,\ell)} + \|\phi\|_{L^2(0,\ell)} + \|f\|_{L^2(0,\lambda;L^2(0,\ell))}\right), \tag{2.5}$$

where $C > 0$ *depends on* α*,* λ*, and* λ_1*.*

Proof. Evaluating formula (2.3) at $t = \lambda$ yields

$$\Phi_n = \phi_n E_\alpha(\mathrm{i}s_n\lambda^\alpha) - \mathrm{i}\int_0^\lambda (\lambda-\tau)^{\alpha-1} E_{\alpha,\alpha}(\mathrm{i}s_n(\lambda-\tau)^\alpha)\,(p_n + f_n(\tau))\,d\tau.$$

Let

$$A_n = -\mathrm{i}\int_0^\lambda (\lambda-\tau)^{\alpha-1} E_{\alpha,\alpha}(\mathrm{i}s_n(\lambda-\tau)^\alpha)\,d\tau.$$

Then,

$$\Phi_n = \phi_n E_\alpha(\mathrm{i}s_n\lambda^\alpha) + A_n p_n - \mathrm{i}\int_0^\lambda (\lambda-\tau)^{\alpha-1} E_{\alpha,\alpha}(\mathrm{i}s_n(\lambda-\tau)^\alpha)\,f_n(\tau)\,d\tau.$$

Since $s_n > 0$, the argument of the Mittag–Leffler function is non–zero. Moreover, the function $E_{\alpha,\alpha}(z)$ is continuous and does not vanish in the considered sector of the complex plane. Therefore, there exists a constant $c > 0$ such that:

$$\left|E_{\alpha,\alpha}(\mathrm{i}s_n(\lambda-\tau)^\alpha)\right| \geq c, \qquad 0 \leq \tau \leq \lambda.$$

Consequently,

$$|A_n| \geq c\int_0^\lambda (\lambda-\tau)^{\alpha-1} d\tau = \frac{c}{\alpha}\lambda^\alpha > 0.$$

Hence, the coefficient A_n is bounded away from zero, and the above relation can be solved for p_n. Using the boundedness of the Mittag–Leffler functions, we obtain

$$|p_n| \leq C\left(|\Phi_n| + |\phi_n| + \int_0^\lambda |f_n(\tau)|\,d\tau\right).$$

Finally, applying Parseval's identity yields the stability estimate (2.5). □

Remark 2.1. *Estimate* (2.5) *demonstrates that the inverse source problem is* conditionally stable*, which is characteristic of the inverse problems governed by fractional-order Schrödinger parabolic differential equations.*

3. FDS for the inverse problem

Let the space and time domains be discretized as follows:

$$x_n = nh, \quad n = 0, 1, \ldots, M, \qquad \text{and} \qquad t_k = k\tau, \quad k = 0, 1, \ldots, N,$$

where $h = \frac{\ell}{M}$ and $\tau = \frac{T}{N}$. The L1 scheme approximated for the Caputo derivative formula (1.5) at $t = t_{k+1}$ is

$${}_0^C D_t^\alpha w_j^{n+1} \approx \frac{1}{\tau^\alpha \Gamma(2-\alpha)} \sum_{j=0}^{k} b_j \left(w_j^{k+1-j} - w_j^{k-j}\right), \tag{3.1}$$

where $b_j = (j+1)^{1-\alpha} - j^{1-\alpha}$. In formula (1.1), the diffusion operator is $\left(a(x)\frac{\partial w(t,x)}{\partial x}\right)_x$.

$$\left(\frac{\partial}{\partial x}\left(a(x)w_x\right)\right)_n^k \approx \frac{1}{h^2}\left[a_{n+\frac{1}{2}}(w_{n+1}^k - w_n^k) - a_{n-\frac{1}{2}}(w_n^k - w_{n-1}^k)\right], \tag{3.2}$$

with $a_{n\pm\frac{1}{2}} = a(x_{n\pm\frac{1}{2}})$. Using formulas (3.1) and (3.2) in formula (1.1), we can obtain

$$\mathrm{i}\frac{1}{\Gamma(2-\alpha)\tau^\alpha}\sum_{j=0}^{k-1} b_j\left(w_n^{k-j} - w_n^{k-j-1}\right) - \frac{1}{h^2}\left[a_{n+\frac{1}{2}}(w_{n+1}^n - w_n^k) - a_{n-\frac{1}{2}}(w_n^k - w_{n-1}^k)\right] = p(x_n) + f(t_k, x_n), \tag{3.3}$$

where $\mu = \tau^\alpha\Gamma(2-\alpha)/h^2$, and

$$\delta_x^2 w_n^k = \frac{w_{n+1}^k - 2w_n^k + w_{n-1}^k}{h^2} \tag{3.4}$$

denotes the standard second-order central difference operator in space. Now, we will establish the unconditional stability and convergence of the present FDS. Let $h = \Delta x$ denote the spatial mesh size. The discrete L^2 norm is defined by

$$\|s\|^2 = h\sum_{j=1}^{M-1}|s_j|^2 = (s, s),$$

where (s, r) denotes the corresponding discrete inner product defined by

$$(s, r) = h\sum_{j=1}^{M-1} s_j r_j.$$

Lemma 3.1. *The L1 coefficients*

$$b_j = (j+1)^{1-\alpha} - j^{1-\alpha}, \quad k \geq 0,$$

satisfy

$$b_j > 0, \quad b_j > b_{j+1}, \quad \sum_{j=0}^{k} b_j = (j+1)^{1-\alpha}.$$

Proof. The proof follows directly from the monotonicity of the function $x^{1-\alpha}$ for $0 < \alpha \leq 1$. □

Lemma 3.2 (Discrete fractional energy inequality)**.** *For any grid function* $\{w^k\}$*,*

$$\sum_{j=0}^{k} b_j(w^{k+1-j} - w^{k-j}, w^{k+1}) \geq \frac{1}{2}\left(\|w^{k+1}\|^2 - \|w^k\|^2\right).$$

Proof. Using summation by parts and the positivity of b_j, we get

$$(w^{k+1} - w^k, w^{k+1}) \geq \frac{1}{2}(\|w^{k+1}\|^2 - \|w^k\|^2),$$

while the remaining terms are nonnegative due to Lemma 3.1. □

Remark 3.1. *In the proof of Theorem 3.2, the discrete fractional energy inequality (Lemma 3.2) is applied to establish stability. Since the diffusion coefficient $a(x)$ is variable, the standard discrete Laplacian must be modified to a weighted form:*

$$(L_m w)_n = a_{n+\frac{1}{2}}\delta_x^2 w_n - a_{n-\frac{1}{2}}\delta_x^2 w_n,$$

where $a_{n\pm 1/2}$ are the values of $a(x)$ at the half-grid points. This weighting ensures that the coercivity of the discrete operator is preserved, i.e., the contribution of w_n to the discrete energy functional properly reflects the spatially varying diffusion. Consequently, when Lemma 3.2 is applied, the inequality

$$\sum_{j=0}^{k} b_j(w^{k+1-j} - w^{k-j}, w^{k+1}) \geq \frac{1}{2}\left(\|w^{k+1}\|^2 - \|w^k\|^2\right)$$

remains valid, with the discrete inner product implicitly incorporating the weights $a_{n\pm 1/2}$. This highlights how the variable diffusion affects the discrete energy while maintaining stability.

Remark 3.2. *Lemma 3.2 holds under the assumption of uniform time steps $\tau_k = k\tau$ for all k. For non-uniform time steps, the L1-type coefficients b_j depend on the varying step sizes, and the discrete fractional energy inequality requires a more careful analysis; in general, Lemma 3.2 cannot be directly applied without modification.*

3.1. Stability analysis

Before proceeding to the stability proof, we note that the imaginary unit i in eq (3.3) does not affect the norm of the discrete solution in the standard L^2-type discrete energy functional. Specifically, taking the discrete inner product of both sides of (3.3) with $\overline{w_n^{k+1}}$ (the complex conjugate) and applying the real part operator $\Re(\cdot)$ eliminates i, ensuring that the resulting energy estimate involves only real non-negative quantities. This justifies the use of the discrete energy method for establishing stability, despite the presence of the complex coefficient.

Theorem 3.1 (Unconditional stability)**.** *The fully discrete FDS for the time-fractional inverse Schrödinger problem is unconditionally stable in the discrete L^2-norm.*

Proof. Consider the fully discrete scheme

$$\mathrm{i}\sum_{j=0}^{k} b_j(w_n^{k+1-j} - w_n^{k-j}) - \mu\left(a_{n+\frac{1}{2}}\delta_x w^k_{n+\frac{1}{2}} - a_{n-\frac{1}{2}}\delta_x w^k_{n-\frac{1}{2}}\right) = \tau^\alpha\Gamma(2-\alpha)f_n^k.$$

Taking the discrete inner product with w^{k+1} and summing over $j = 1, \ldots, N-1$, we obtain

$$\mathrm{i}\sum_{j=0}^{k} b_j(w^{k+1-j} - w^{k-j},\ w^{k+1}) - \mu(\mathcal{L}_m w^k, w^{k+1}) = \tau^\alpha\Gamma(2-\alpha)(f^k, w^{k+1}),$$

where $\mathcal{L}_m$ denotes the discrete diffusion operator. By discrete integration by parts, the operator $\mathcal{L}_m$ satisfies:

$$(\mathcal{L}_m v, v) = \sum_{n=0}^{M-1} a_{n+\frac{1}{2}}\left|\delta_x v_{n+\frac{1}{2}}\right|^2 \geq 0, \quad \forall v.$$

Hence, the mixed term $(\mathcal{L}_m w^k, w^{k+1})$ is estimated using the Cauchy–Schwarz and Young inequalities:

$$\left|(\mathcal{L}_m w^k, w^{k+1})\right| \leq \varepsilon\|\delta_x w^k\|^2 + C_\varepsilon\|w^{k+1}\|^2.$$

Taking the imaginary part of the inner-product equation and applying Lemma 3.2 for the convolution coefficients $\{b_j\}$ yields

$$\|w^{k+1}\|^2 - \|w^k\|^2 \leq C\tau^\alpha\|f^k\|^2.$$

Applying the Cauchy–Schwarz and Young inequalities to the right-hand side, we arrive at

$$\|w^{k+1}\|^2 \leq \|w^k\|^2 + C\tau^\alpha\|f^k\|^2.$$

Iterating the above inequality with respect to k gives

$$\|w^{k+1}\|^2 \leq \|w^0\|^2 + C\tau^\alpha \sum_{j=0}^{k} \|f^j\|^2,$$

which proves that the numerical solution remains bounded independently of the step sizes τ and h. This completes the proof. □

3.2. Convergence analysis

Let $W_n^k = w(t_k, x_n)$ demonstrate the exact solution evaluated at grid points, and define the global error

$$e_n^k = W_n^k - w_n^k.$$

Lemma 3.3 (Local truncation error)**.** *Assume* $w(t,x) \in C^2([0,T]; H^4(0,\ell))$*. Then the local truncation error satisfies:*

$$\|\mathcal{T}^k\| \leq C(\tau^{2-\alpha} + h^2).$$

Here, T^k denotes the local truncation error of a numerical scheme at the k-th time step.

Proof. The L1 approximation for the Caputo derivative operator has accuracy $O(\tau^{2-\alpha})$, while the central difference approximation of the spatial operator is second-order accurate. □

Theorem 3.2 (Convergence)**.** *Let* $w(t,x)$ *be the exact solution of the continuous problem and* w_n^k *be the numerical solution. Then*

$$\|w(t_k, \cdot) - w_n^k\| \leq C(\tau^{2-\alpha} + h^2), \quad 0 \leq k \leq N.$$

Proof. Deriving the numerical scheme from the exact discrete equation gives the error equation

$$\mathrm{i}\sum_{j=0}^{k} b_j(e^{k+1-j} - e^{k-j}) - \mu\mathcal{L}_m e^k = \tau^\alpha\Gamma(2-\alpha)\mathcal{T}^k.$$

Applying the same energy argument as in Theorem (3.1) and using Lemma (3.3), we have

$$\|e^{n+1}\|^2 \leq \|e^n\|^2 + C(\tau^{2-\alpha} + h^2)^2.$$

A discrete Grönwall inequality completes the proof. □

Remark 3.3. *Since the governing eq (1.1) contains the imaginary unit* i*, the solution* $w(t, x)$ *is complex-valued. In the numerical implementation, the discrete solution is stored as complex numbers, and all operations are performed in the complex domain. For clarity, one can equivalently consider the real and imaginary parts separately: if* $w = u + \mathrm{i}v$*, then the scheme can be written in terms of the coupled real system for* (u, v)*. However, the discrete energy functional used in the stability analysis of Theorem 3.2 naturally accounts for the complex inner product* $\langle w, w\rangle = \sum_n w_n\overline{w_n}$*, which implicitly incorporates the contributions of both the real and imaginary components. Therefore, the stability estimate holds for the full complex-valued solution without requiring additional separation of real and imaginary parts. In MATLAB, the complex solution* w_n^k *can be stored directly as a complex array, and all linear algebra operations (e.g., multiplications, inner products) automatically handle both real and imaginary components.*

Remark 3.4. *While this section focuses on the error analysis for the state variable* $w(t, x)$*, it is important to note that, in the context of the inverse problem, the convergence of the unknown source* $p(x)$ *is equally significant. Let* $w_{approx}(\lambda, x)$ *denote the numerical solution at the measurement time* $t = \lambda$*. The reconstruction of* $p(x)$ *typically relies on a relation of the form*

$$p_{approx}(x) = \frac{w_{approx}(\lambda, x) - other\ terms}{\lambda^{\alpha}},$$

so that the error in w *at* $t = \lambda$ *propagates directly into the error of* $p_{approx}(x)$*. Thus, one can bound*

$$\|p(x) - p_{approx}(x)\| \leq C\,\|w(\lambda, x) - w_{approx}(\lambda, x)\|,$$

where C *depends on the inverse formula and the diffusion coefficient* $a(x)$*. A rigorous derivation of this bound is an important extension and will be included in future work. This remark emphasizes the connection between the state variable error and the accuracy of the reconstructed source.*

Remark 3.5. *One of the main computational challenges of L1-type FDSs for fractional PDEs is the nonlocality of the Caputo derivative, which requires storing all previous time steps. For a uniform grid with* N *time steps and* M *spatial points, the memory requirement is* $O(N \cdot M)$*, and the total computational complexity is* $O(M \cdot N^2)$*. In the present implementation, no acceleration techniques such as the sum-of-exponentials (SOEs) approximation or fast convolution methods were employed; the full L1 memory is retained. For larger* N*, one can significantly reduce memory and computational cost using these acceleration strategies, which is an important direction for future work.*

Remark 3.6. *As the diffusion coefficients* $a(x) = x^2$ *and* $a(x) = x^3$ *vanish at the boundary* $x = 0$*, the solution gradients may become steep in that region. On a uniform spatial grid, these sharp gradients could reduce the local accuracy, potentially affecting the global* $2-\alpha$ *convergence order. To accurately capture the boundary behavior, a graded mesh with finer spatial steps near* $x = 0$ *or adaptive temporal steps can be employed. Such non-uniform grids concentrate points where the solution changes rapidly, thereby maintaining the theoretical convergence order. In the present work, to avoid the singularity at* $x = 0$*, we have considered the modified coefficients* $a(x) = x^2 + 1$ *and* $a(x) = x^3 + 1$*, which are strictly positive, ensuring uniform ellipticity and allowing a uniform grid to be sufficient for the intended accuracy.*

4. Numerical results

In this section, two examples are presented to validate the proposed FDM for the FOSPDEs. Numerical experiments are carried out to verify the stability and accuracy of the given method. A manufactured exact solution satisfying the IBC is employed to evaluate the numerical error. An algorithm of the FDM for the FOSPDEs can be given as follows:

(1) **Initialization of parameters:** Set the fractional order $\alpha \in (0, 1]$, spatial domain $[0, \ell]$, and final time T. Choose the number of spatial and temporal grid points M and N, and define

$$h = \frac{\ell}{M}, \qquad \tau = \frac{T}{N}.$$

Construct the spatial grid $x_n = nh$, $n = 0, 1, \ldots, M$, and time grid $t_k = k\tau$, $k = 0, 1, \ldots, N$.

(2) **Compute L1 fractional weights:** For the CFOD, compute the L1 coefficients

$$b_j = (j + 1)^{1-\alpha} - j^{1-\alpha}, \qquad j = 0, 1, \ldots, N - 1.$$

Define the scaling constant

$$C_\alpha = \frac{1}{\Gamma(2 - \alpha)\tau^\alpha}.$$

(3) **Apply the initial condition:** Initialize the numerical solution matrix

$$w_n^0 = (t_0^{\alpha+3} - 1)\sin(x_n), \qquad n = 0, 1, \ldots, M.$$

(4) **Construct the finite difference system:** For each time level $k = 1, 2, \ldots, N$, form the tridiagonal matrix A corresponding to the spatial operator

$$-\frac{\partial}{\partial x}\left(a(x)\frac{\partial w}{\partial x}\right),$$

where $a(x) = x^3 + 1$. The coefficients are computed using

$$a_{n+\frac{1}{2}} = (x_n + \tfrac{h}{2})^3 + 1, \qquad a_{n-\frac{1}{2}} = (x_n - \tfrac{h}{2})^3 + 1.$$

(5) **Evaluate the fractional history term and source function:** Compute the memory term

$$H_n^k = \sum_{j=1}^{k-1} b_{j+1}\left(w_n^{k+1-j} - w_n^{k-j}\right),$$

and evaluate the source function

$$f(t, x) = \left(\frac{\mathrm{i}}{6}\Gamma(\alpha + 4)t^3 + (x^3 + 1)t^{\alpha+3} - 1\right)\sin x - 3x^2(t^{\alpha+3} - 1)\cos x.$$

Then, assemble the right-hand side vector.

(6) **Solve the linear system and compute the error:** Solve the system

$$A\, w^{k+1} = \text{RHS}$$

to obtain the numerical solution at the time level $k + 1$. After completing all time steps, compute the maximum error

$$E = \max_{n,k} \left| w(x_n, t_k) - w_{\text{exact}}(x_n, t_k) \right|,$$

where the exact solution is

$$w_{\text{exact}}(t, x) = (t^{\alpha+3} - 1) \sin x.$$

Using the FDM for the inverse problem FOSPDEs, we will apply two numerical examples.
Example 1: This example presents an application of model (1.1) with IBVCs:

$$\begin{cases} a(x) = x^2 + 1, \\ p(x) = -(x^2 + 1)\sin x, \\ w(0, x) = -\sin x, \quad x \in [0, \pi], \\ w\left(\frac{1}{2}, x\right) = \left((\frac{1}{2})^{\alpha+3} - 1\right) \sin x, \quad x \in [0, \pi], \quad \lambda = \frac{1}{2}, \\ w(t, 0) = 0, \quad w(t, \pi) = 0, \quad t \in [0, 1], \\ f(t, x) = \left(\dfrac{1}{6} t^3 \Gamma(\alpha + 4)\mathrm{i} + (x^2 + 1) t^{\alpha+3}\right) \sin x - 2x(t^{\alpha+3} - 1)\cos x. \end{cases} \tag{4.1}$$

Using the FDM and formula (3.3), we can get the following Figures 1–11 and Table 1. Figure 1 shows the absolute error between the exact and numerical solutions obtained by the FDM. The small magnitude and smooth distribution of the error indicate that the numerical scheme provides an accurate approximation over the entire computational domain. The heatmap visualization provides a clear physical interpretation of the solution evolution, where the gradual transition of color intensity reflects the nonlocal temporal memory effect associated with the fractional order $\alpha = 0.75$ in Figure 7, leading to slower diffusion compared to the classical case where $\alpha = 1$ in Figure 8.

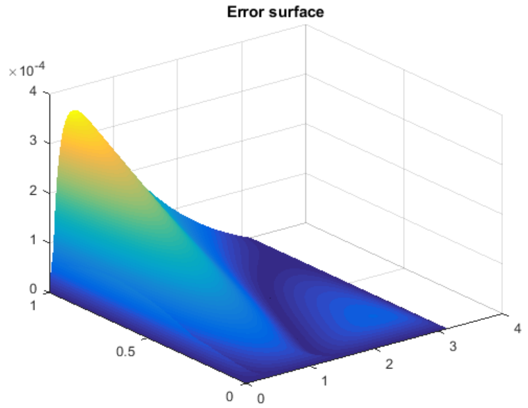

Figure 1. Three-dimensional error surface plot for $\alpha = 0.5$ obtained using $M = 100$ spatial grid points and $N = 200$ time steps ($h = \pi/M$, $\tau = 1/N$) on the domain $0 \le x \le \pi$, $0 \le t \le 1$, $a(x) = x^2 + 1$.

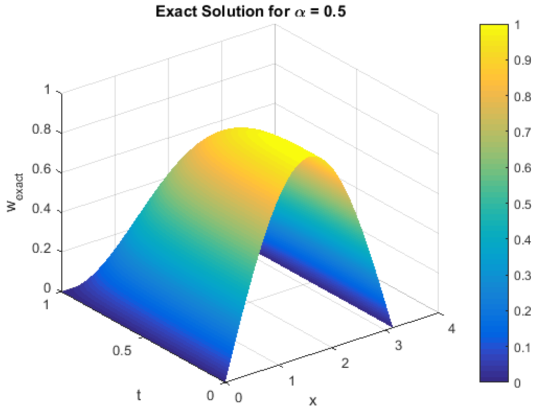

Figure 2. Three-dimensional exact surface plot for $\alpha = 0.5$ on the domain $0 \leq x \leq \pi$, $0 \leq t \leq 1$, $u(t,x) = \left(t^{\alpha+3} - 1\right)\sin x$.

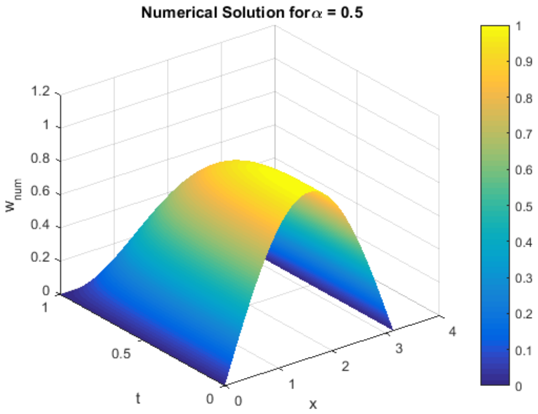

Figure 3. Three-dimensional approximate solution surface plot for $\alpha = 0.5$ obtained using $M = 100$ spatial grid points and $N = 200$ time steps ($h = \pi/M$, $\tau = 1/N$) on the domain $0 \leq x \leq \pi$, $0 \leq t \leq 1$, $a(x) = x^2 + 1$.

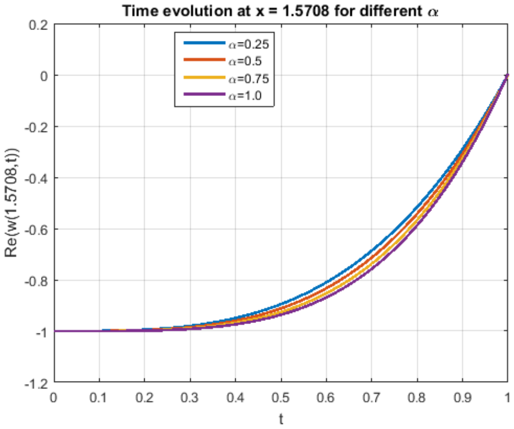

Figure 4. Comparison of numerical solutions for diverse fractional orders $\alpha = 0.25, 0.5, 0.75$, and 1, illustrating the influence of the fractional order on the solution behavior.

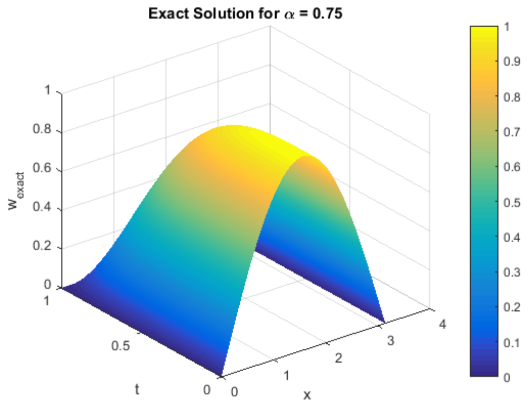

Figure 5. Three-dimensional surface plot of the exact solution corresponding to $\alpha = 0.75$, illustrating the space–time behavior of the fractional inverse parabolic model on $0 \leq x \leq \pi$ and $0 \leq t \leq 1$.

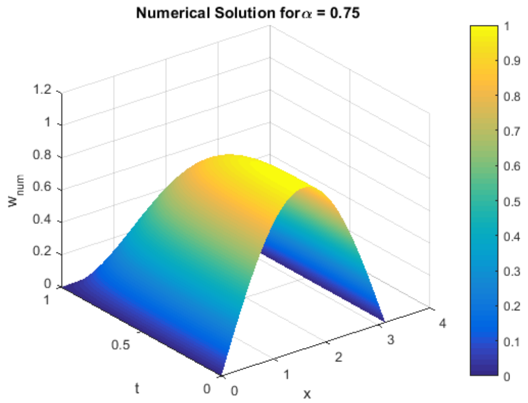

Figure 6. Three-dimensional surface plot of the approximate solution corresponding to $\alpha = 0.75$, illustrating the space–time behavior of the fractional inverse parabolic model on $0 \leq x \leq \pi$ and $0 \leq t \leq 1$.

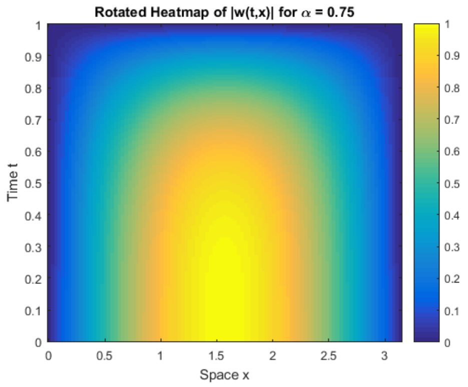

Figure 7. Heatmap representation of the numerical solution for $\alpha = 0.75$ obtained with $M = 100$ and $N = 200$ ($h = \pi/M$, $\tau = 1/N$) on $0 \leq x \leq \pi$, $0 \leq t \leq 1$. Warmer colors correspond to higher solution amplitudes, while cooler colors indicate lower values, illustrating the gradual diffusion and long-memory effects inherent to fractional inverse parabolic dynamics.

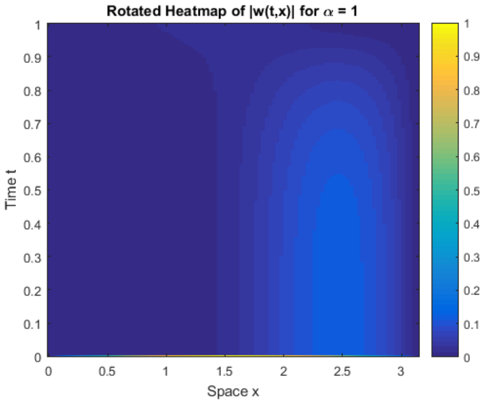

Figure 8. Heatmap representation of the numerical solution for $\alpha = 1$ obtained with $M = 100$ and $N = 200$ ($h = \pi/M$, $\tau = 1/N$) on $0 \leq x \leq \pi$, $0 \leq t \leq 1$. Warmer colors indicate higher solution amplitudes, while cooler colors correspond to lower values, revealing the gradual diffusion and long-memory behavior characteristic of fractional inverse parabolic dynamics.

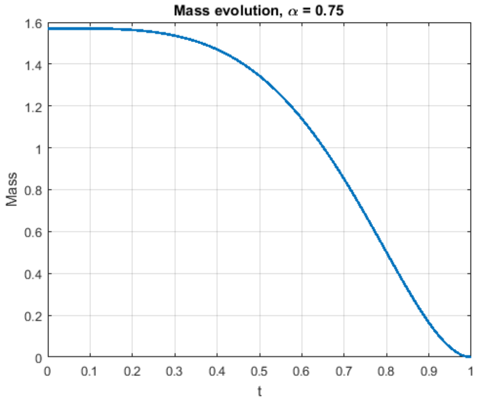

Figure 9. Time evolution of the discrete mass corresponding to $\alpha = 0.75$, illustrating the non-conservative and memory-dependent nature of the fractional inverse parabolic model.

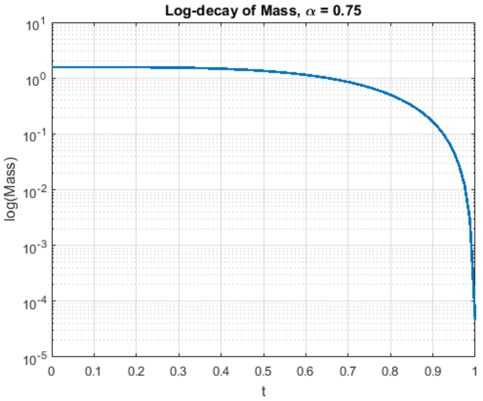

Figure 10. Logarithmic decay representation of the discrete mass decay for $\alpha = 0.75$, highlighting the slow, memory-driven dissipation induced by the CFOD.

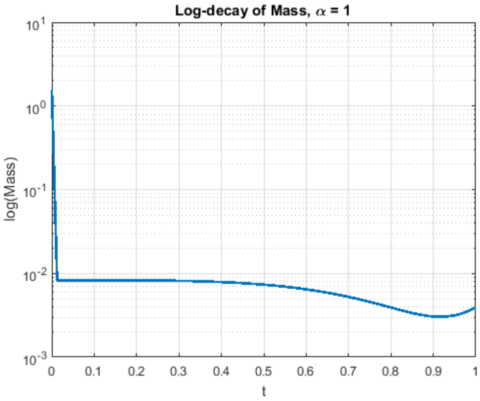

Figure 11. Logarithmic representation of the discrete mass decay for $\alpha = 1$, highlighting the slow, memory-driven dissipation induced by the integer-order derivative.

Table 1. Comparison of CPU time, memory usage, error norms, and fractional memory cost (FMC) for different α and N

α	N	CPU Time (s)	Memory (MB)	Max Error (L_∞)	L2 Error	FMC
0.25	50	1.11×10^{-1}	4.16×10^{-2}	3.18×10^{-4}	1.41×10^{-4}	1.00
	100	6.56×10^{-2}	8.24×10^{-2}	3.12×10^{-4}	1.37×10^{-4}	0.59
	150	1.05×10^{-1}	1.23×10^{-1}	3.11×10^{-4}	1.36×10^{-4}	0.94
	200	1.54×10^{-1}	1.64×10^{-1}	3.10×10^{-4}	1.35×10^{-4}	1.39
0.50	50	1.78×10^{-2}	4.16×10^{-2}	4.62×10^{-4}	2.20×10^{-4}	1.00
	100	4.35×10^{-2}	8.24×10^{-2}	3.58×10^{-4}	1.66×10^{-4}	2.44
	150	8.58×10^{-2}	1.23×10^{-1}	3.40×10^{-4}	1.54×10^{-4}	4.82
	200	1.41×10^{-1}	1.64×10^{-1}	3.33×10^{-4}	1.49×10^{-4}	7.91
0.75	50	2.09×10^{-2}	4.16×10^{-2}	2.04×10^{-3}	7.48×10^{-4}	1.00
	100	4.96×10^{-2}	8.24×10^{-2}	9.06×10^{-4}	3.92×10^{-4}	2.37
	150	8.75×10^{-2}	1.23×10^{-1}	6.22×10^{-4}	2.92×10^{-4}	4.19
	200	1.41×10^{-1}	1.64×10^{-1}	5.34×10^{-4}	2.47×10^{-4}	6.74
1	50	2.01×10^{-2}	4.16×10^{-2}	1.31×10^{-2}	3.94×10^{-3}	1.00
	100	9.60×10^{-2}	8.24×10^{-2}	6.81×10^{-3}	2.10×10^{-3}	4.77
	150	8.81×10^{-2}	1.23×10^{-1}	4.63×10^{-3}	1.47×10^{-3}	4.38
	200	1.39×10^{-1}	1.64×10^{-1}	3.53×10^{-3}	1.15×10^{-3}	6.92

The logarithmic decay plot (Figure 10) of the mass provides complementary information to the standard mass evolution curve. Although the mass evolution in Figure 9 illustrates the global temporal behavior of the solution on a linear scale, the log-decay representation reveals the long-time dissipation rate more clearly. For $\alpha = 0.75$, the nearly linear trend in the logarithmic scale indicates a slow, history-dependent decay, which is characteristic of fractional-order dynamics. This behavior contrasts with the classical case where $\alpha = 1$, where a steeper slope is observed, corresponding to faster mass dissipation. The agreement between the mass evolution and its logarithmic decay confirms the numerical stability of the proposed scheme and the physical consistency of the fractional inverse parabolic model. Three-dimensional surface plots, heatmaps, and log-decay error curves confirm excellent agreement between exact and numerical solutions for various α values.

Remark 4.1. *The inverse problems are well known to be sensitive to measurement errors. To assess the robustness of the proposed method, it would be valuable to include a "noisy data" test where the measurement at* $t = \lambda$ *is perturbed, e.g.,*

$$w_{noisy}(\lambda, x) = w(\lambda, x) + \varepsilon(x), \quad \|\varepsilon(x)\| \ll 1. \tag{4.2}$$

This allows us to examine how errors in the observed data propagate into the reconstruction of the unknown source $p(x)$ *and to quantify the stability of the numerical scheme under realistic measurement conditions. Such a study could be included in future work or as an additional numerical experiment.*

Figure 12 shows the effect of additive Gaussian noise on the exact solution of the fractional model for different noise intensities. The computational domain is discretized using $M = 50$ spatial grid points and $N = 100$ temporal grid points.

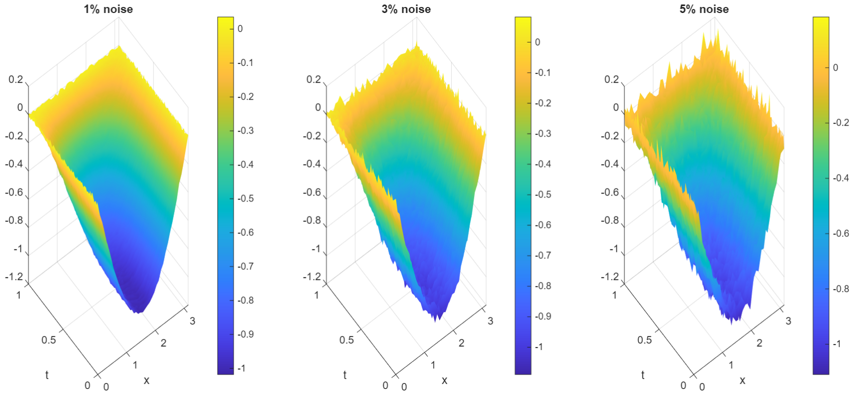

Figure 12. Comparison of noisy observational data for different noise levels (1%, 3%, and 5%) added to the exact solution for $\alpha = 0.75$. The results illustrate the sensitivity of the inverse problem to measurement errors and demonstrate the robustness of the proposed numerical scheme.

Example 4.2: This example presents an application of model (1.1) with IBVCs:

$$\begin{cases} a(x) = x^3 + 1, \\ p(x) = -(x^3 + 1)\sin x, \\ w(0, x) = -\sin x, \quad x \in [0, \pi], \\ w\left(\frac{1}{2}, x\right) = \left((\frac{1}{2})^{\alpha+3} - 1\right)\sin x, \quad x \in [0, \pi], \quad \lambda = \frac{1}{2}, \\ w(t, 0) = 0, \quad w(t, \pi) = 0, \quad t \in [0, 1], \\ f(t, x) = \left(\dfrac{1}{6} t^3 \Gamma(\alpha + 4)\mathrm{i} + (x^3 + 1)t^{\alpha+3}\right)\sin x - 3x^2(t^{\alpha+3} - 1)\cos x. \end{cases} \tag{4.3}$$

By using the FDM formula (3.3), we can get the following Figures 13 and 14, and Table 2. The FDM described in formula (3.3) is applied to solve the inverse fractional problem numerically. The scheme is implemented with discretization parameters M (spatial grid points) and N (time steps), where the spatial step size is $h = \pi/M$ and the temporal step size is $\tau = 1/N$. Numerical results are presented for the case with diffusion coefficient $a(x) = x^3 + 1$. Figure 13 displays the exact solution of the fractional inverse parabolic problem for $\alpha = 0.5$, while Figure 14 shows the corresponding numerical approximation obtained with $M = 100$ and $N = 200$. Both solutions are computed on the domain $0 \le x \le \pi$, $0 \le t \le 1$. The visual comparison illustrates the accuracy of the proposed numerical scheme in capturing the solution behavior.

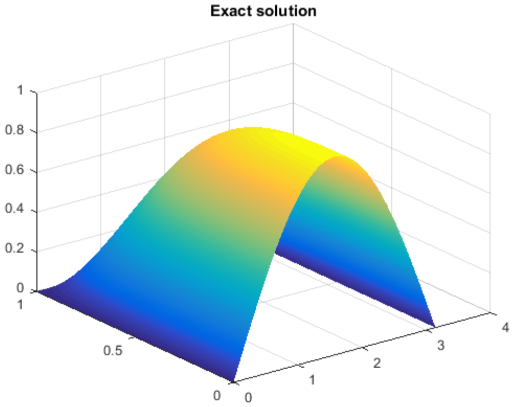

Figure 13. Exact solution of the fractional inverse parabolic problem for $\alpha = 0.5$ with diffusion coefficient $a(x) = x^3 + 1$, computed on the domain $0 \le x \le \pi$, $0 \le t \le 1$.

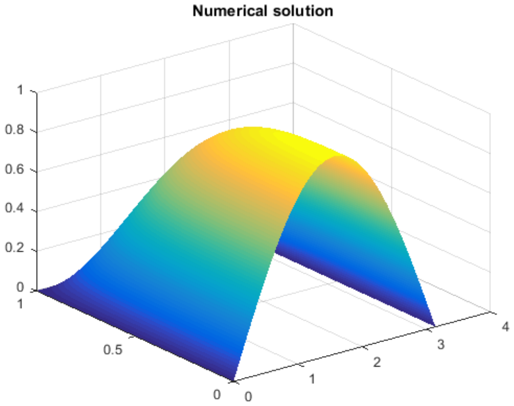

Figure 14. Numerical solution of the fractional inverse parabolic problem for $\alpha = 0.5$ with diffusion coefficient $a(x) = x^3 + 1$, computed on the domain $0 \le x \le \pi$, $0 \le t \le 1$ using $M = 50$ spatial grid points and $N = 100$ time steps ($h = \pi/M$, $\tau = 1/N$).

To quantify the convergence and accuracy of the method, a comprehensive error analysis is performed. Table 1 tabulates the maximum values of error norms and the corresponding convergence rates for different values of the fractional order α and for both diffusion coefficients

$$a(x) = x^2 + 1 \ \ and \ \ a(x) = x^3 + 1.$$

The error is evaluated as

$$E_\infty(h, \tau) = \max_{k,n} |e_n^k|,$$

and the experimental convergence rate in time is computed via

$$\text{Rate} = \log_2\left(\frac{E_\infty(h,\tau)}{E_\infty(h/2,\tau/2)}\right).$$

The results in Table 2 demonstrate that the method achieves the expected convergence behavior, with errors decreasing systematically as the mesh is refined. Notably, the convergence rate approaches the theoretical order as α varies, confirming the stability and reliability of the FDS.

Table 2. Maximum error $E_\infty(h,\tau)$ and convergence rates for different fractional orders α with $a(x) = x^2 + 1$ and $a(x) = x^3 + 1$

α	N	E_∞ ($a(x) = x^2 + 1$)	Rate	E_∞ ($a(x) = x^3 + 1$)	Rate
0.25	25	2.65709×10^{-4}	–	3.46517×10^{-4}	–
	50	8.42417×10^{-5}	1.657	9.05595×10^{-5}	1.936
	100	2.63508×10^{-5}	1.677	2.39356×10^{-5}	1.920
	200	8.15789×10^{-6}	1.692	6.40710×10^{-6}	1.901
0.50	25	1.72708×10^{-3}	–	9.24905×10^{-4}	–
	50	6.30006×10^{-4}	1.455	3.32391×10^{-4}	1.476
	100	2.27490×10^{-4}	1.470	1.18686×10^{-4}	1.486
	200	8.15791×10^{-5}	1.480	4.22413×10^{-5}	1.490
0.75	25	9.25622×10^{-3}	–	4.67673×10^{-3}	–
	50	3.98096×10^{-3}	1.217	1.98499×10^{-3}	1.236
	100	1.69386×10^{-3}	1.233	8.38119×10^{-4}	1.244
	200	7.16636×10^{-4}	1.241	3.53184×10^{-4}	1.247
1	25	4.42768×10^{-2}	–	2.49230×10^{-2}	–
	50	2.29279×10^{-2}	0.949	1.30080×10^{-2}	0.938
	100	1.16690×10^{-2}	0.974	6.65621×10^{-3}	0.967
	200	5.88584×10^{-3}	0.987	3.36871×10^{-3}	0.983

Figure 13 shows that the analytical solution is given by

$$w(x,t) = (t^{\alpha+3} - 1)\sin(x),$$

which satisfies the prescribed initial and boundary conditions of the problem. The surface plot illustrates the smooth variation of the solution with respect to both space and time. As time increases, the amplitude of the solution evolves according to the fractional time-dependent term $t^{\alpha+3}$. The spatial structure is governed by the sinusoidal function $\sin(x)$, producing a wave-like profile along the spatial domain. Figure 14 illustrates the approximate numerical solution of the fractional inverse problem. The numerical approximation is obtained using the FDM. In this approach, the spatial derivative terms are discretized using finite difference approximations on a uniform spatial grid, while the fractional time derivative is approximated using the L1 discretization scheme.

The computational domain is divided into discrete spatial and temporal grid points, and the resulting difference equations are solved sequentially at each time level. The surface plot depicts the evolution of the numerical solution with respect to both space and time. The obtained solution preserves the smooth structure of the underlying analytical model and reflects the diffusion behavior governed by the spatially varying coefficient $a(x) = x^3 + 1$. The figure demonstrates that the finite difference scheme effectively captures the dynamics of the fractional inverse parabolic equation across the entire computational domain.

Remark 4.2. *In Table 2, the convergence rates for different values of* α *and different steps of* N *and* M *in Example 4.1 and Example 4.2 show a slight drop compared to the expected value. This deviation is likely due to the nonlinear behavior introduced by the diffusion coefficient* $a(x) = x^2 + 1$ *and* $a(x) = x^3 + 1$*, which produces sharper gradients near* $x = 0$ *and affects the discrete approximation locally. As a result, the global convergence rate is marginally reduced. Using a graded spatial mesh near the boundary could mitigate this effect, but for the present study, the uniform grid provides sufficiently accurate results for demonstration purposes.*

5. Conclusions

In this study, an FDM for inverse source problems relying on time-fractional-order Schrödinger equations is analyzed and proposed. The fractional time derivative operator is interpreted in the Caputo sense, allowing for the inclusion of physically meaningful initial conditions. Under appropriate regularity assumptions on the exact solution and problem data, exact stability estimates and prior error bounds are constructed in appropriate discrete norms. It is proven that the approximate solution converges to the exact solution with a well-defined degree of accuracy in both time and space discretizations. Furthermore, it is shown that the inverse source problem is unconditionally stable and provides a continuous dependence of the reconstructed source term on the measured final time data. Numerical examples are in full agreement with the theoretical analysis and confirm the efficiency and reliability of the suggested scheme. Additionally, the "memory effect" observed in the heatmaps (Figures 7 and 8) reflects the intrinsic fractional-order dynamics: past states influence the present evolution, leading to slower diffusion or persistence of spatial patterns compared to integer-order models. Summarizing this physical implication helps the reader connect the numerical results to the underlying physics. Finally, future work should explicitly consider high-dimensional extensions (2D or 3D domains), as real-world applications often require solving inverse fractional Schrödinger-type problems in multiple spatial dimensions. This sets a clear direction for practical and theoretical extensions of the proposed method. The proposed method is flexible and can be extended to more general linear and nonlinear models, including the Gross-Pitaevskii equation, which governs Bose-Einstein condensates and is a nonlinear Schrödinger-type model, as well as to other fractional-order models based on the Caputo derivative or alternative fractional operators.

Author contributions

The authors contributed equally to this work. All authors read and approved the final manuscript.

Use of Generative-AI tools declaration

The authors declare that they have not used Artificial Intelligence (AI) tools in the creation of this article.

Acknowledgments

The authors are very grateful to the anonymous referees for their careful reading and valuable comments that led to the improvement of this manuscript.

Conflict of interest

The authors declare no conflicts of interest.

References

1. F. Ozbag, M. Modanli, On the stability estimates and numerical solution of fractional order telegraph integro-differential equation, *Phys. Scr.*, **96** (2021), 094008. https://doi.org/10.1088/1402-4896/ac0a2c
2. R. Ashurov, M. Shakarova, Time-dependent source identification problem for a fractional Schrödinger equationwith the Riemann–Liouville derivative, *Ukr. Math. J.*, **75** (2023), 997–1015. https://doi.org/10.1007/s11253-023-02243-1
3. A. Oulmelk, L. Afraites, A. Hadri, An inverse problem of identifying the coefficient in a nonlinear time-fractional diffusion equation, *Comput. Appl. Math.*, **42** (2023), 65. https://doi.org/10.1007/s40314-023-02206-z
4. Y. F. Patel, M. Izadi, Exact solutions of the generalized time-fractional order Burgers–Huxley equation with a robust semi-analytical technique, *J. Umm Al-Qura Univ. Appl. Sci.*, 2025. https://doi.org/10.1007/s43994-025-00283-w
5. Y. F. Patel, M. Izadi, An analytical investigation of nonlinear time-fractional Schrödinger and coupled Schrödinger-KdV equations, *Results Phys.*, **70** (2025), 108137, https://doi.org/10.1016/j.rinp.2025.108137
6. A. Rayal, S. R. Verma, Two-dimensional Gegenbauer wavelets for the numerical solution of tempered fractional model of the nonlinear Klein-Gordon equation, *Appl. Numer. Math.*, **174** (2022), 191–220, https://doi.org/10.1016/j.apnum.2022.01.015
7. H. M. Ahmed, New generalized Jacobi Galerkin operational matrices of derivatives: An algorithm for solving multi-term variable-order time-fractional diffusion-wave equations, *Fractal Fract.*, **8** (2024), 68, https://doi.org/10.3390/fractalfract8010068
8. S. Ahmed, S. Jahan, K. S. Nisar, Haar wavelet based numerical technique for the solutions of fractional advection diffusion equations, *J. Math. Comput. Sci.*, **34** (2024), 217–233. http://doi.org/10.22436/jmcs.034.03.02
9. M. Modanli, B. Bajjah, Double Laplace decomposition method and FDM of time-fractional Schrödinger pseudoparabolic partial differential equation with Caputo derivative, *J. Math.*, **2021** (2021), 7113205, https://doi.org/10.1155/2021/7113205
10. S. E. Chorfi, F. Et-tahri, L. Maniar, M. Yamamoto, Forward and backward problems for abstract time-fractional Schr¨odinger equations, *Comm. Nonlinear Sci. Numer. Simul.*, **157** (2026), 109758. https://doi.org/10.1016/j.cnsns.2026.109758

11. A. Ashyralyev, A. U. Sazaklioglu, Investigation of a time-dependent source identification inverse problem with integral overdetermination, *Numer. Funct. Anal. Optim.*, **38** (2017), 1276–1294. https://doi.org/10.1080/01630563.2017.1316996
12. C. Ashyralyyev, M. Dedeturk, FDM for the inverse elliptic problem with Dirichlet condition, *Contemp. Anal. Appl. Math.*, **1** (2013), 132–155.
13. A. Ashyralyev, M. Urun, Stability of time-dependent source identification problem for Schrödinger differential equations, *TWMS J. Pure Appl. Math.*, **13** (2022), 245–255.
14. L. Baudouin, A. Mercado, An inverse problem for Schrödinger equations with discontinuous main coefficient, *Appl. Anal.*, **87** (2008), 1145–1165. https://doi.org/10.1080/00036810802140673
15. M. Modanli, B. Bajjah, Double Laplace decomposition method and FDM of time-fractional Schrödinger pseudoparabolic partial differential equation with Caputo derivative, *J. Math.*, **1** (2021), 7113205.
16. M. Modanli, B. Bajjah, S. Kuşulay, Two numerical methods for solving the Schrödinger parabolic and pseudoparabolic partial differential equations, *Adv. Math. Phys.*, **2022** (2022), 6542490. https://doi.org/10.1155/2022/6542490
17. C. Mattschas, M. Puplauskis, C. Toebes, V. Sharoglazova, J. Klaers, Inverse solving the Schrödinger equation for precision alignment of a microcavity, *Phys. Rev. Research*, **7** (2025), 013296. https://doi.org/10.1103/PhysRevResearch.7.013296
18. K. Oishi, Y. Hashizume, T. Nakao, K. Kashima, Extraction of implicit field cost via inverse optimal Schrödinger bridge, *SICE J. Control Meas. Syst. Integr.*, **18** (2025), 2490332. https://doi.org/10.1080/18824889.2025.2490332
19. S. E. Chorfi, A. Hasanov, R. Morales, Identification of source terms in the Schrödinger equation with dynamic boundary conditions from final data, *Z. Angew. Math. Phys.*, **76** (2025), 127. https://doi.org/10.1007/s00033-025-02505-x
20. E. Shivanian, A. Jafarabadi, M. J. Huntul, A local meshless technique for recovering dual forms of time-varying sources in the nonlocal inverse heat equation, *Results Appl. Math.*, **28** (2025), 100673. https://doi.org/10.1016/j.rinam.2025.100673
21. M. J. Huntul, Inverse source problems for multi-parameter space-time fractional differential equations with bi-fractional Laplacian operators, *AIMS Math.*, **9** (2024), 32734–32756. https://doi.org/10.3934/math.20241566
22. M. J. Huntul, I. Tekin, M. Izadi, Utilizing septic B-splines for inverse recovery in sixth-order Boussinesq-Love equations, *Comp. Appl. Math.*, **45** (2026), 227. https://doi.org/10.1007/s40314-026-03626-3
23. J. Chung, S. Gazzola, Computational methods for large-scale inverse problems: A survey on hybrid projection methods, *SIAM Rev.*, **66** (2024), 205–284. https://doi.org/10.1137/21M1441420
24. S. M. Sayed, A. S. Mohamed, E. M. Abo-Eldahab, Y. H. Youssri, A compact combination of second-kind Chebyshev polynomials for Robin boundary value problems and Bratu-type equations, *J. Umm Al-Qura Univ. Appl. Sci.*, **11** (2025), 766–783. https://doi.org/10.1007/s43994-024-00184-4

25. M. A. Abdelkawy, W. M. Abd-Elhameed, S. S. Alzahrani, A. G. Atta, A. Biswas, Numerical solutions via shifted Pell polynomials for third-order Rosenau–Hyman and Gilson–Pickering equations, *Mathematics*, **14** (2026), 582. https://doi.org/10.3390/math14030582
26. W. M. Abd-Elhameed, H. M. Ahmed, M. A. Zaky, R. M. Hafez, A new shifted generalized Chebyshev approach for multi-dimensional sinh-Gordon equation *Phys. Scr.*, **99** (2024), 095269. https://doi.org/10.1088/1402-4896/ad6fe3
27. R. Gorenflo, A. A. Kilbas, F. Mainardi, S. V. Rogosin, *Mittag-Leffler Functions, Related Topics and Applications*, Berlin: Springer, 2020.